Nanoscale

PAPER

View Article Online
View Journal | View Issue

Cite this: *Nanoscale*, 2026, **18**, 5371

Albumin coating of magnetic nanoparticles for imaging, tracking and delivery through biological barriers

Annalisa Caputo,†[a,b] Alessia Nito,†[a,c] Lucia Giampetruzzi,[d] Antonio Gaballo,[a] Anna Grazia Monteduro,[a,h] Riccardo Di Corato,[d] Clara Piccirillo,[a] Concetta Nobile,[a] Andrea Ragusa,[e] Marco Di Paola,[f] Giuseppe Gigli,[a,g] Giuseppe Maruccio,[a,h] Amilcare Barca[g] and Alessandra Quarta*[a]

The advent of nanotechnology in biotechnology and medicine has accelerated the development of nanomaterials as innovative tools for diagnostics, therapy, and drug delivery. Despite their versatility, many nanoparticle systems fail *in vivo* due to their limited ability to traverse biological barriers, resulting in off-target distribution, rapid clearance, or undesired bioaccumulation. Structural parameters—including size and surface chemistry—critically shape nanoparticle biodistribution and fate. Albumin, the most abundant serum protein, naturally acts as a long-circulating carrier capable of transporting diverse molecules across biological interfaces. Owing to its stability and favorable pharmacokinetics, albumin has emerged as a valuable component of drug delivery systems and nanoformulations. In this work, we introduce albumin-coated magnetic zinc ferrite nanoparticles as a platform designed to overcome these limitations. Our results show that an albumin coating markedly enhances nanoparticle stability and provides a versatile shell that can encapsulate lipophilic drugs or incorporate tracking agents. Functionally, the albumin-coated nanoparticles demonstrate efficient penetration and transport across biological barriers *in vitro*: they successfully enter 3D breast tumor spheroids and show measurable translocation across an enterocyte monolayer model. These findings highlight the potential of albumin-coated magnetic zinc ferrite nanoparticles as multifunctional carriers for targeted delivery and biomedical imaging, and support the relevance of 3D models for assessing nanoparticle transport and therapeutic efficacy.

Received 7th October 2025,
Accepted 21st January 2026

DOI: 10.1039/d5nr04238k

rsc.li/nanoscale

1. Introduction

Nanomedicine is identified as a multidisciplinary research area that encompasses biotechnology, nanotechnology, and medicine, and whose applications include diagnostic devices and biosensors, molecular imaging and drug/gene delivery, as well as regenerative medicine. As an example, the scale of nanotechnology tools, such as nanoparticles (NPs), offers multiple benefits for overcoming the constraints of conventional drug administration methods through target-oriented and release-controlled transport. NPs have shown great potential for enhancing the solubility and stability of encapsulated cargos, as well as prolonging the circulation time and enhancing cellular uptake.[1]

Among nanomaterials, inorganic nanoparticles, such as those composed of metals and oxides, have been designed and tested as diagnostic, sensing or therapeutic tools for human diseases, mainly cancer and neurodegenerative diseases.[2] Research efforts have been focused on shaping materials with tunable features and physico-chemical properties, and to make them safe or stimuli responsive.[3] To cite some examples, gold and ferrite nanoparticles attracted broad interest thanks to their physical properties, ease of preparation and good biocompatibility. They have been widely investigated as imaging probes by means of computed tomography (CT) and magnetic resonance imaging (MRI), and as therapeutic tools by deliver-

[a]*Institute of Nanotechnology, National Research Council, via Monteroni, Lecce, 73100, Italy. E-mail: alessandra.quarta@nanotec.cnr.it*
[b]*Department of Mathematics and Physics, University of Salento, via Monteroni, Lecce, 73100, Italy*
[c]*Department of Engineering for Innovation, University of Salento, via Monteroni, Lecce, 73100, Italy*
[d]*Institute for Microelectronics and Microsystems, National Research Council, Lecce, 73100, Italy*
[e]*Department of Life Sciences, Health and Health Professions, Link Campus University, Via del Casale di San Pio V, 44, 00165 Rome, Italy*
[f]*Institute of Clinical Physiology, National Research Council, via Monteroni, 73100 Lecce, Italy*
[g]*Department of Experimental Medicine, University of Salento, Via Monteroni, Lecce, 73100, Italy*
[h]*Omnics Research Group, Department of Mathematics and Physics, University of Salento, INFN Sezione di Lecce, Via per Monteroni, 73100 Lecce, Italy*
†These authors have contributed equally to this work.

ing drugs or burning cancer cells upon optical activation or magnetic stimulation.[4,5]

Despite broad interest, so far only a few candidates have successfully entered the clinic,[6] and in Europe only two clinical trials are currently ongoing with inorganic nanoparticles (https://euclinicaltrials.eu/search-clinical-trials-reports/). Beyond the huge costs of clinical research, the main limitations for the clinical translation of nanomaterials generally include unfavorable biodistribution and clearance, and undesired side effects.[7]

This low degree of success depends on the structural features of the nanomaterials, such as size, surface charge, chemical composition and stability, and the interactions they establish with the biological environment. In fact, upon injection or administration, nanoparticles meet and interact with the biological barriers that should be overcome, *i.e.* the natural defenses against the influx of foreign materials and organisms.[8,9] They include specialized epithelia that coat organs, the epidermis, the blood–brain barrier and the immune system cells devoted to the sequestration of non-self-materials. In the case of nanomaterials envisaged for cancer treatment, the tumor's anatomy and microenvironment themselves represent a barrier due to an irregular vascular structure and poor lymphatic drainage, which limit penetration to distant areas.[10,11]

Thus, the design of nanoparticles and nanomaterials intended for biomedical applications should carefully consider the features of the environment to be faced. One of the approaches proposed to make the nanoparticles "invisible" to the immune system and capable of crossing biobarriers is to make them biomimetic while having an optimal size to limit rapid sequestration or clearance.[12,13]

Albumin is the most abundant serum protein with a concentration ranging from 35 to 55 g L^{-1} and it is involved in the transport of endogenous and exogenous molecules.[14] It can diffuse into and out of blood vessels and cross biological barriers, such as the blood–brain barrier (BBB), *via* transcytosis. It displays multiple binding sites thus allowing for the transport of a wide range of molecules and substances in the blood, mainly lipophilic molecules, such as fatty acids, hormones, vitamins and drugs.[15] Human serum albumin (HSA) is synthesized by the liver and released in the bloodstream with a turnover of approximately 25 days.[16] Its molecular weight is around 67 kDa and consists of three domains, which are in turn formed by two subdomains. In addition to HSA, bovine serum albumin (BSA) is widely used in research as it displays 76% sequence homology with the human protein and is much cheaper. Indeed, thanks to its natural role as molecular cargo in addition to having a long circulatory half-life, favorable pharmacokinetics and stability, albumin has been investigated and proposed as a carrier system for drugs.[17]

Several examples of albumin–drug conjugates and albumin nanoparticles have been developed, such as the methotrexate–albumin conjugate[18,19] described for the first time in 1997, and more recently albumin nanoparticles loaded with either doxorubicin[20] or paclitaxel[21] for tumor drug delivery. Abraxane®, the commercial name for nanoparticle albumin bound paclitaxel was approved by the Food and Drug Administration (FDA) in 2005 for breast cancer treatment, while in 2022, Nanozora®, an albumin-binding nanobody against human TNF-α, was approved in Japan for the treatment of rheumatoid arthritis.[22] These data confirm the strong interest in albumin-based technologies and nanoformulations as alternative delivery solutions. Albumin has also been used as a coating agent for inorganic nanoparticles to either improve cell targeting or drug delivery.[23] The group of Chen prepared HSA-coated iron oxide nanoparticles for cell targeting, while Hiremath *et al.* reported the development of HSA-coated iron oxide nanoparticles functionalized with folic acid for the combined delivery of 5-fluorouracil and curcumin.[24,25] Nanogold–albumin conjugates have also been proposed for the delivery of therapeutic agents and for diagnostic imaging.[26,27]

Herein we propose the use of albumin as an organic coating for zinc ferrite magnetic nanoparticles, prepared by thermal decomposition, to cross biological barriers and act as a delivery agent. The synthesis of the nanoparticles, performed without the use of toxic solvents, is followed by the albumin coating step. In this study bovine serum albumin (BSA) was used because of its easy availability and cheapness, but HSA has been tested as well. The albumin-coated magnetic nanoparticles (MNP@BSA) show great stability and versatility. Indeed, the fluorescent labelling of albumin and cisplatin loading of the albumin shell have been reported: the former to track the nanoparticles upon cellular internalization, and the latter to investigate the delivery performance of a drug with poor water solubility. The presence of a magnetic domain provides MR susceptibility to the whole nanostructure, the magnetic properties of which have also been investigated. Upon characterization of the morpho-structural features of MNP@BSA, *in vitro* studies were performed to assay their capacity to deliver cisplatin, in addition to their cytocompatibility. Hydrogel-embedded 3D tumor models of breast cancer and monolayers of Caco2 enterocyte-like cells were used as models of biological barriers to be overcome. The aim of this work is the multiscale validation of a nanoplatform, moving beyond simple *in vitro* testing. Specifically, the study contributes by addressing key translational barriers in nanomedicine, strengthening the case for protein-coated inorganic nanoparticles as a theranostic system and advancing 3D tumor modeling for drug delivery evaluation.

2. Materials and methods

2.1. Chemicals

Tetraethylene glycol, zinc(II) acetylacetonate, iron(III) acetylacetonate, bovine serum albumin (BSA), human serum albumin (HSA), 1-ethyl-3-(3-dimethylaminopropyl)carbodiimide (EDC), rhodamine 101, the BCA assay kit, *cis*-diaminoplatinum, dimethyl sulfoxide (DMSO), agarose, blue Coomassie staining, glutaraldehyde, Dulbecco's modified Eagle's medium (DMEM), fetal bovine serum (FBS), phosphate

buffered saline (50 mM, pH 7.4), penicillin, streptomycin, and β-agarase from *Pseudomonas atlantica* were obtained from Merck (Milan, IT) and used as received. The live/dead viability/cytotoxicity kit was purchased from Thermo Fisher Scientific. The CellTiter-Glo® 3D cell viability assay (Promega, Madison, WI 53711 USA). Human cancer cells were purchased from the American Type Culture Collection (ATCC). Ultrapure water with a conductivity of 18.2 MΩ cm was used in all experiments.

2.2. Synthesis of MNPs

$ZnFe_2O_4$ nanoparticles (from this point on referred to as MNP in the text) were prepared through a thermal decomposition method, according to the protocol described in the literature and as depicted in Scheme 1 that summarises the main steps of the present study, from the nanoparticle synthesis and functionalization with albumin to their characterization and *in vitro* validation.[28]

In detail, 268 mg of zinc(II) acetylacetonate (equal to 1 mmol) and 712 mg of iron(III) acetylacetonate (equal to 2 mmol) were dissolved in 10 mL of tetraethylene glycol. The solution was degassed under vacuum at 100 °C for 30 min and then the temperature was brought to 210 °C under a N_2 atmosphere and continuous stirring. After 2 h the temperature was increased to 305 °C and kept at this temperature for 1 h. Finally, the reaction flask was cooled to room temperature under air. The sample was then washed with a mixture of ethanol and acetone (1 : 3 volume ratio) and centrifuged at 1500*g* for 15 min; the pellet was dissolved in ethanol.

2.3. Functionalization of MNPs with albumin

For surface functionalization with BSA, 50 mL of the protein solution in PBS (at concentrations ranging from 2 to 5 mg mL^{-1}) were added to $ZnFe_2O_4$ nanoparticles (1 mL 25 μM) and left under stirring for 24 h at 4 °C. Then, the nanoparticles were washed several times on centrifugal filters (100 kDa molecular weight cut-off) to remove unbound BSA. The presence of excess BSA was monitored by measuring the absorbance at 280 nm of the buffer fractions collected. Finally, the nanoparticle solution was passed through a Sephadex column and filtered using 0.2 μm sterile filters under a laminar flow hood to reduce the contamination risk prior to storage in the fridge.

To make the nanoparticles fluorescent, rhodamine 101 was bound to the BSA shell. Fluorophore solution (1 mM in DMSO) and 50 mM EDC in PBS were added to the 5 μM MNP-BSA solution. The mixture was stirred for 3 h at room temperature. Then, the samples were washed on centrifugal filters until the buffer volumes collected were fluorescence-free.

2.3.1. Loading of *cis*Pt. *cis*-Diammineplatinum(II) dichloride (*cis*Pt) (either 75, 150 or 300 μL of a 20 mM solution in DMSO) was added to the ethanol suspension of nanoparticles (1.5 mL, 15 μM). The suspension was left under stirring for 30 min at room temperature. Then, the BSA solution (50 mL, 5 mg mL^{-1} in PBS) was added, and the final suspension was sonicated for 3 min in an ice bath by using a probe sonicator (50% power, Bandelin Sonopuls). The turbid suspension turned clear and was left under stirring overnight at 4 °C.

To remove the excess BSA and the unbound *cis*Pt, five washing steps were performed using centrifugal filters followed by purification through a Sephadex column.

2.4. Characterization of MNPs

2.4.1. Elemental analysis by inductively coupled plasma–atomic emission spectroscopy. The concentration of the nanoparticles, the Fe/Zn ratio and the amount of Pt molecules

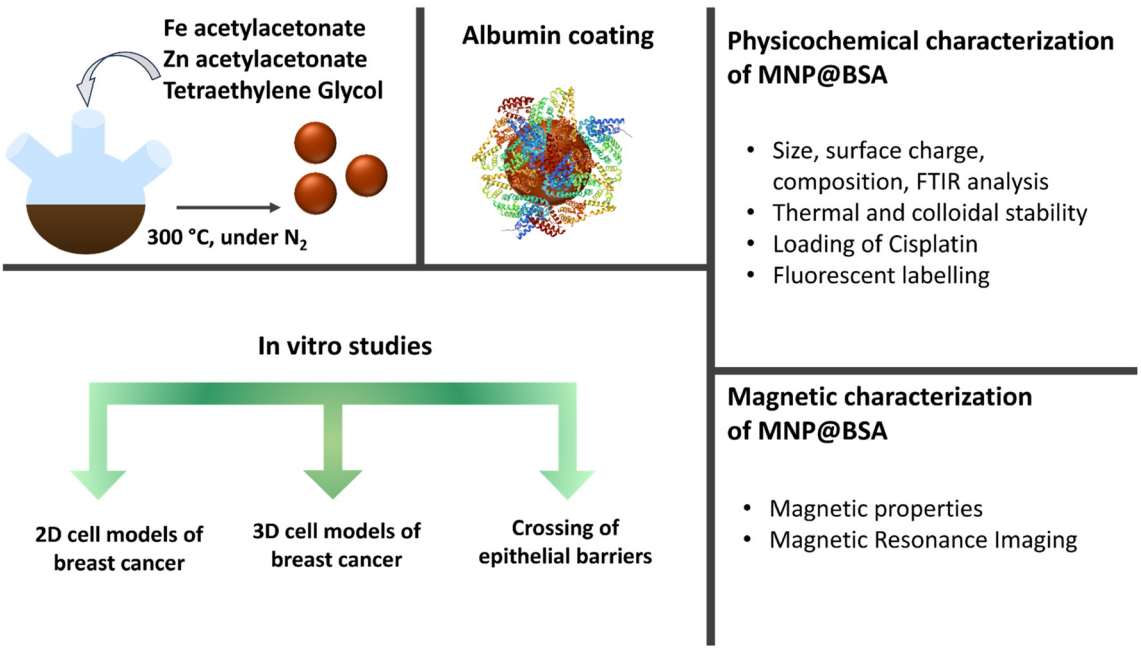

Scheme 1 Preparation procedure for MNP@BSA, followed by the characterization steps and *in vitro* studies.

linked per nanoparticle were estimated *via* elemental analysis using a Varian 720-ES inductively coupled plasma atomic emission spectrometer (ICP-AES). The calibration curves for Fe, Pt and Zn were prepared, and the relative amount of metal per sample was estimated upon acidic digestion in HNO_3/HCl (1/3) solution.

2.4.2. Transmission electron microscopy (TEM). Low-magnification TEM images were recorded using a JEOL Jem1400plus microscope (Jeol Ltd, Tokyo, Japan) operating at an accelerating voltage of 120 kV. A drop of the nanoparticle solution was cast on a carbon-coated copper grid and left to dry overnight before imaging.

For ultrastructural imaging of breast cancer spheroids grown inside the agarose hydrogel, the embedded spheroids were washed with PBS after exposure for 24 h to MNP@BSA. They were then recovered after treatment with β-agarase and fixed with 2.5% glutaraldehyde in 0.1 M cacodylate buffer at 4 °C for 60 min, as already described.[29] The fixed specimens were washed three times and then incubated in 1% osmium tetroxide solution (in cacodylate buffer) for 1 h. Next, the cells were washed again and dehydrated with 25%, 50%, 75% and 100% acetone. Three steps of infiltration in a mixture of resin and acetone (1 : 2, 1 : 1 and 2 : 1 ratios) were performed. The specimens were then embedded in 100% resin and left to polymerize at 60 °C for 48 h. Ultrathin sections (75 nm thick) were cut on an ultramicrotome (RMC PowerTome PT-XL, Boeckeler Instruments, Inc., Tucson, AZ, USA) and observed under the electron microscope.

2.4.3 X-ray diffraction and Raman spectroscopy analyses. The as-prepared $ZnFe_2O_4$ NPs were analysed by X-ray diffraction (XRD) to determine their phase composition; the diffraction patterns were acquired with a Rigaku SmartLab instrument, with Cu Kα radiation (50 mA and 40 kV). The acquisition was performed for the 2θ interval between 25 and 65°, with a step scan of 0.02° and an acquisition rate of 1° min^{-1}. The acquired data were compared to the JCPDS-PDF 01-077-0011 standard file.

Raman analysis was performed using an Oxford Instrument (alpha300) with a 633 nm laser.

2.4.4. Dynamic light scattering. Dynamic light scattering (DLS) and zeta potential measurements were performed to estimate the average hydrodynamic diameter and surface charge of the nanoparticles by using a Nano ZS90 Zetasizer (Malvern, USA) equipped with a 4.0 mW He–Ne laser operating at 633 nm and with an avalanche photodiode detector. The measurements were performed in PBS (pH 7.4, 50 mM). The samples were measured soon after preparation in PBS and after incubation in the cell medium.

2.4.5. Fourier-transform infrared spectroscopy. Fourier-transform infrared (FT-IR) spectra were recorded in transmittance mode on a Jasco 6300 spectrometer (Jasco Corporation, Tokyo, Japan) between 4000 and 500 cm^{-1} with 40 scans and a resolution of 4 cm^{-1} and analyzed with Spectra Manager software (Jasco). The measurements were performed by directly depositing the hydrogels onto the ATR crystal. The spectrum of each sample was acquired against a background obtained with the crystal without any sample. All analyses were carried out at room temperature.

2.4.6. Thermogravimetric analysis. Thermal stability was assessed by thermogravimetric analysis (TGA) using SDT Q600 equipment (TA Instruments, New Castle, DE, USA) with a heat ramp of 5 °C min^{-1} and an air flow rate of 100 mL min^{-1}. The as-prepared nanoparticles dissolved in ethanol were dried in air, while BSA-coated nanoparticles were lyophilized before the analysis.

2.4.7. Magnetic characterization. The magnetization of the samples was measured by using a vibrating sample magnetometer (VSM, Cryogenic Ltd). Measurements were performed on MNPs as dry samples over the field range of −1 T to 1 T at 300 K. For each sample, the results were shown as specific magnetization (units of emu g^{-1}).

2.4.8. Magnetic resonance imaging. Magnetic resonance imaging was performed using a Bruker ICON scanner. The scanner was interfaced with ParaVision software for preclinical MRI research. The nanoparticles were dispersed in 1% agarose and stored at 4 °C. All samples were imaged by (i) a T_2 multislice multiecho (MSME) sequence with a TR of 3000 ms, multiple TE from 12 to 90 ms, and a flip angle of 180° and (ii) a T_1 echo planar sequence (EPI) with a TR of 2000 ms, a TE of 16 ms, multiple TI from 37 to 1162 ms, and a flip angle of 45°.

2.4.9. Bicinchoninic acid assay. The bicinchoninic acid (BCA) assay was used to estimate the amount of BSA linked per nanoparticle. A calibration curve with free BSA molecules in the concentration range from 0 to 100 μg mL^{-1} was prepared. Then the BCA solution was added both to the BSA calibration points and to the samples. At the end of the incubation time, the NP samples were centrifuged using Microcon filters (100 kDa MWCO) to eliminate interference from the NP absorbance. The collected solutions were optically measured at 562 nm by using a CLARIOstar Plus BMG LABTECH microplate reader.

2.4.10. Gel electrophoresis. Electrophoretic characterization was carried out by running the nanoparticles through 1% agarose gel in TBE buffer (pH 8.0). After the gel was run (1 h at 100 V), Coomassie staining was performed to detect the BSA protein shell coating the nanoparticles.

2.5. Cellular assays

2.5.1 2D breast cancer cell culture. MCF-7 breast cancer cells were used following the ATCC maintenance recommendations. The cells were grown at 37 °C and 5% CO_2 in DMEM high glucose supplemented with L-glutamine, penicillin, streptomycin, and 10% heat-inactivated fetal bovine serum.

2.5.2 3D breast cancer cell cultures. Two different preparation approaches were used; the first one, based on low attachment culture plates and specific culture medium, leads to the formation of mammospheres in suspension; the second one, based on agarose hydrogel, leads to the formation of tumor spheroids embedded in a matrix that mimics the extracellular microenvironment.

In the first approach, MCF-7 tumor spheroids were obtained by using the MammoCult™ medium (human) kit

(StemCell Technologies) according to the manufacturer's suggested protocol for human breast cancer cell lines. In brief, MCF-7 cells were grown as monolayers until they reached 80–90% confluency. On day 1, cells were scraped and resuspended in 10 mL of complete MammoCult™ medium (Stemcell Technologies, catalog #05620). After centrifugation at 500*g* for 3 min at room temperature (15–25 °C), the pellet was resuspended as a single cell suspension in 2 mL of complete MammoCult™ medium. The cells were then counted and seeded at a density of 2×10^4 MCF-7 cells per well into a 6-well ultra-low adherent plate (catalog #27145). The plate was incubated in a humidified incubator with 5% CO_2, at 37 °C for 5 days before harvesting.

In the second approach, MCF-7 tumor spheroids were obtained by seeding cells in an agarose hydrogel matrix (0.2% in complete cell medium). 2×10^4 MCF-7 cells were seeded in 24 well plates and incubated in a humidified incubator with 5% CO_2, at 37 °C, following the protocol described in a recent paper.[29] The growth of the tumor spheroids was monitored daily under an optical microscope for up to 10 days.

2.5.3 Biocompatibility assays and internalization of MNP@BSA. The biocompatibility of the BSA-coated nanoparticles was assessed by means of standard viability assays for both 2D and 3D cultures. The internalization was followed by means of fluorescent imaging, ultrastructural analysis and elemental analysis.

MTT assay of 2D cell cultures. To assess the biocompatibility of the nanoparticles in 2D cell cultures, the standard MTT assay was performed. In detail, MCF-7 cells (1×10^4 cells per 200 μL of complete medium) were seeded in each well of a 96-well plate. After 24 h of incubation at 37 °C, fresh medium containing MNP@BSA at three concentration points, 100, 300, and 900 nM, was added. The cells were incubated for 3, 24, and 72 h. Next, the medium was removed, and the cells washed twice with PBS (50 mM, pH 7.4). 1 mL of serum-free medium containing 3-(4,5-dimethyl-2-thiazolyl)-2,5-diphenyl-2*H*-tetrazolium bromide (1 mg mL^{-1}) was then added to each well. After 2 h of incubation at 37 °C, the dark insoluble formazan obtained was dissolved in DMSO (2 mL). The absorbance signal at 570 nm was correlated to the percentage of vital cells by comparing data from treated cells to those of the control cells. The assay was independently replicated three times, with each test point analyzed in triplicate.

Live/dead assay of 3D cell cultures. The viability of 3D tumor models was investigated by using a live/dead viability/cytotoxicity kit (Thermo Fisher Scientific Inc., Waltham, MA, USA). Briefly, the activity of intracellular esterase induces non-fluorescent, cell-permeant calcein acetoxymethyl ester to become fluorescent after hydrolysis, giving green fluorescence to the viable 3D breast tumors. On the other hand, ethidium homodimer enters and binds nucleic acids only in damaged cells, producing a red fluorescence that indicates dead cells. As reported in the previous section, 2×10^4 MCF-7 cells per well in a 24-well plate were suspended in the agarose hydrogel matrix. The plate was incubated in a humidified incubator with 5% CO_2, at 37 °C.

The assay was performed at three time points to monitor the viability of the spheroids during their growth and upon incubation with MNP@BSA. In detail, the medium was carefully removed from the plates containing the spheroids and the samples were washed twice with PBS. A phosphate buffer solution containing calcein and ethidium homodimer was then added, and the plate was incubated at 37 °C for 1 h. Then, the solution was replaced with fresh PBS before the fluorescence intensity of both calcein and propidium heterodimer were measured by using the CLARIOstar Plus BMG LABTECH microplate reader. The assay was independently replicated two times, with each test point analyzed in triplicate. Finally, imaging of the samples was performed under a fluorescence microscope (EVOS FLoid Cell Imaging Station, ThermoFisher, Waltham, MA, USA).

CellTiter-Glo® 3D cell viability assay. The CellTiter-Glo® 3D cell viability assay (Promega) was used to determine the number of viable cells in a 3D cell culture of mammospheres treated with either MNP@BSA or MNP@BSA-*cis*Pt. It is based on the quantitation of ATP present in metabolically active cells through the luminescence generated by the ATP-dependent luciferase activity.

2×10^4 MCF-7 cells per well dispersed in Mammocult medium were added to a 6-well ultra-low adherent plate. The plate was incubated in a humidified incubator with 5% CO_2, at 37 °C for 5 days. After incubation with the nanoparticles and subsequent rinsing steps, the mammospheres were transferred back into the well plates (see the next section for further details). Then, the assay reagent was added to the plate and upon vigorous mixing, the plate was left under stirring 25 min prior to the luminescence being measured by using a CLARIOstar Plus BMG LABTECH microplate reader. An ATP standard curve was set by using ATP sodium salt. Soon after the measurement, the BCA assay was performed to estimate the protein content and normalize the luminescence measurement with respect to the amount of protein.

2.5.4. Delivery of *cis*Pt to tumor spheroids by MNP@BSA. After two weeks of growth, the agarose-embedded spheroids were incubated with MNP@BSA, MNP@BSA-*cis*Pt or free *cis*Pt at a NP concentration of 200 nM, corresponding to about 10 μM Pt. After 24 h, the medium containing NPs or the free drug was removed and the embedded spheroids were washed several times with PBS before proceeding with the assays.

In the case of the mammospheres, after 4 days of growth, MNP@BSA, MNP@BSA-*cis*Pt or free *cis*Pt (200 nM NP concentration, corresponding to about 10 μM Pt) were added to the well plates. After 24 h, the medium with the spheroids was collected and transferred to a conic tube. After a few minutes, the mammospheres settled down and, after carefully removing the medium, they were washed with PBS before being processed for the CellTiter-Glo® 3D cell viability assay. Each assay was independently replicated two times, with each test point analyzed in triplicate.

2.5.5. Delivery of MNP@BSA across an enterocyte-like epithelial monolayer. Human intestinal epithelial Caco-2 cells (ATCC n. HTB-37™) were grown at 37 °C, under a humidified

atmosphere (5% CO_2 in air), in MEM supplemented with 10% (v/v) FBS, 2 mM L-glutamine, 100 μg mL^{-1} penicillin–streptomycin and 1% (v/v) non-essential amino acid mix solution. The culture medium was replaced every third day (starting from the seeding day) and propagation occurred routinely every 4–5 days. For the experiments, after the third passage of propagation, 0.4×10^5 cells per well were seeded on 12 mm Transwell® inserts (polyethylene terephthalate membrane inserts with 0.4 μm porosity, Corning-Mouser, Assago, MI, Italy) and maintained under continuous growth conditions for up to 21 days post seeding (dps), changing apical and basolateral culture media every 3 days, to obtain a spontaneously differentiated epithelial monolayer ("enterocyte-like"), according to standard Caco-2 cell differentiation protocols.[30,31]

Then, rhodamine-labelled MNP@BSA dissolved in Dulbecco's phosphate buffered saline (D-PBS) were added to the culture medium in the upper (*i.e.* apical) compartment of the transwells, at a final concentration of 50 nM. The cells were then incubated for 0 (*i.e.* T_0 time point, corresponding to 30 min incubation), 1, 3, 5, and 7 days. At each time point, partial volumes of culture media from both the upper (apical) and lower (basolateral) compartments were collected and analyzed using photoluminescence and elemental analysis.

In addition, lysates of cell monolayers were collected and processed for elemental analysis. Samples of cells on transwell inserts were also collected for fluorescent imaging. Photoluminescence measurements were performed using a Cary Eclipse fluorimeter. After the optical measurements, the solutions were lyophilized and then digested in a HCl/HNO_3 (3 : 1) mixture before the Fe content was quantified using a Varian 720-ES ICP-AES spectrometer. Fluorescence images of the cells were taken with an Evos m7000 fluorescence microscope.

2.6. Statistical analysis

All data were analysed using GraphPad software. Data sets were tested for statistical significance using one-way analysis of variance (ANOVA) and *t*-tests. A p value less than 0.05 was considered statistically significant. Data are reported as mean ± standard error of mean of three independent repeats.

3. Results

3.1. Synthesis and functionalization of MNPs

The synthesis of $ZnFe_2O_4$ MNPs was carried out by a thermal decomposition approach.[28] Specifically, iron(III) acetylacetonate and zinc(II) acetylacetonate were used as organometallic precursors, while tetraethylene glycol was used as an organic solvent. Following this procedure, ethanol-soluble nanoparticles with a diameter of about 6–7 nm were obtained.

In the context of this work, BSA (50 mg mL^{-1} in PBS) was used. To encapsulate *cis*Pt within the BSA coating, the drug was added to the functionalization mixture, along with BSA. After BSA coating, the MNPs were purified by washing and size exclusion chromatography.

3.2. Characterization of MNP@BSA

The MNPs were characterized by elemental analysis (ICP-AES), BCA protein assay, electron microscopy, powder X-ray diffraction, Raman spectroscopy, photon correlation spectroscopy, measurement of surface charge, FTIR, TGA and gel electrophoresis. Elemental analysis allowed for the measurement of the concentration of the two metals composing the MNPs, expressed in ppm, and for the estimation of the molar concentration of the MNPs.

As reported in Table 1, the molar ratio between Fe and Zn remains almost unchanged at each step, oscillating between 2.0 and 2.5. This variation, which shows an increase in the Fe content after synthesis, could be associated with a modest loss of Zn atoms from the inorganic core during the washing and purification phases.

The number of BSA molecules bound per MNP was estimated through the BCA protein assay, after determining the concentration of nanoparticles through elemental analysis.

As reported in Table 2, given the initial addition of approximately 150 molecules of BSA per MNP, about 5.6 molecules per MNP were bound to the surface after the purification steps. This value remained almost unchanged, even when cisplatin was encapsulated. By knowing the BSA/MNP molar ratio, the molecular weight of BSA (66.5 kDa) and the estimated mass of the nanoparticles, the BSA/MNP mass ratio could be estimated to be around 9.7. This indicates that the mass contribution of the protein shell is considerably higher than that of the inorganic domain.

The morphology of the MNPs was analyzed by transmission electron microscopy. Fig. 1A and S1A (in the SI) show the morphology of the as-synthesized nanoparticles, while Fig. 1B and S1B show that of the nanoparticles after protein coating. The image in Fig. 1B provides evidence of the higher contrast of the inorganic core (bordered with red dotted circles) compared to that of the organic shell (bordered with green dotted circles). Compared to the pristine nanoparticles, those coated with the protein appear to be distributed in clusters on the TEM grid. Statistical analysis of the inorganic core using Image J reveals an average diameter of 6.9 nm (Fig. 1C), while the thickness of the dry protein shell is around 1.6 nm (Table 2). Interestingly, although the images were acquired with a low-resolution microscope, the lattice fringe patterns of some particles can be observed, as indicated by the red arrows. Fig. 1D shows the diffraction pattern of the NPs. Peaks were detected at 30, 35.4, 42.7, 53.2, 56.7 and 62.1°; these correspond to the $ZnFe_2O_4$ phase, with a spinel-type structure.[32] The

Table 1 Fe/Zn molar ratios in zinc ferrite nanoparticles at each step of preparation

Step	Fe/Zn
Added to the synthesis	2.00
After the synthesis of MNPs	2.06 ± 0.04
After functionalization with BSA	2.14 ± 0.19
After the encapsulation of *cis*Pt	2.52 ± 0.07

Table 2 Molar ratios of BSA/MNP and *cis*Pt/MNP before and after purification, as determined by ICP-AES and BCA assays; values of TEM sizes and hydrodynamic diameter, PDI, and zeta potential of the MNPs at each functionalization step

	BSA/MNP molar ratio					
	Initial	Final	TEM diameter (nm)	Hydrodynamic diameter (nm)	PDI	*z*-Potential (mV)
MNP@BSA	~150	5.6 ± 0.4	Core: 6.9 ± 0.6 Shell: 1.6 ± 0.3	178.9 ± 2.2	0.10 ± 0.02	−11.7 ± 0.3
MNP@BSA-*cis*Pt	~150	5.5 ± 0.3	Core: 6.9 ± 0.6 Shell: 2.6 ± 0.4	183.4 ± 1.3	0.09 ± 0.01	−11.3 ± 0.4

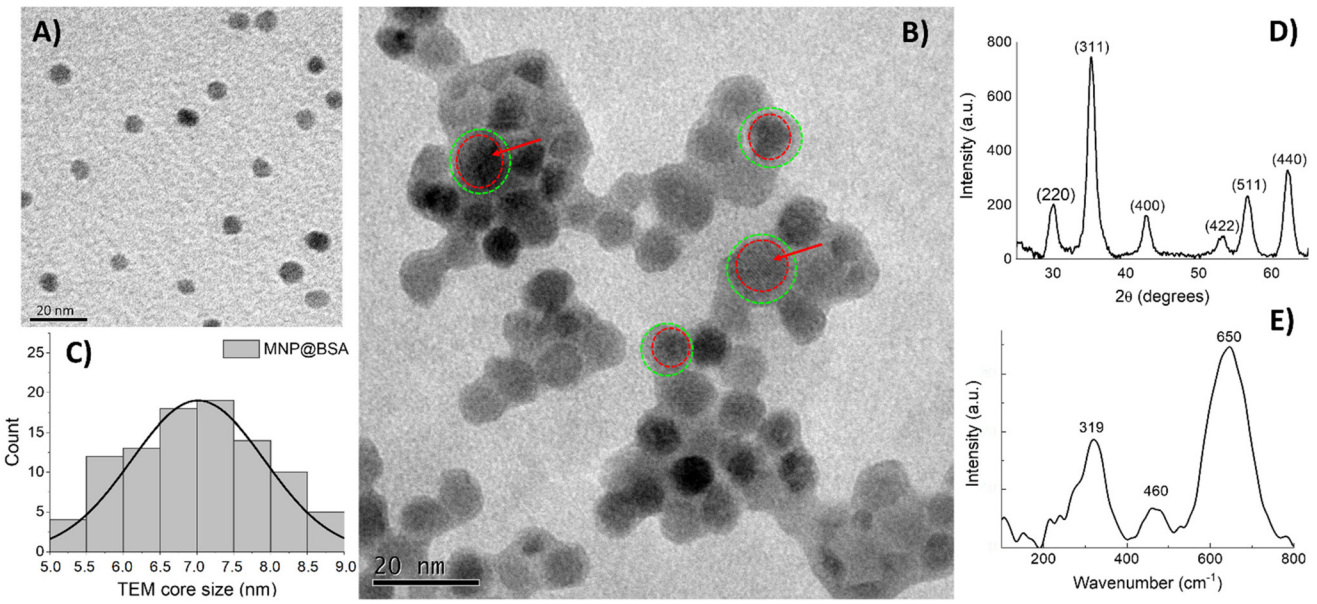

Fig. 1 Morphological and structural characterization of MNP@BSA. TEM images of (A) as-synthesized and (B) BSA-coated magnetic nanoparticles. Scale bar is 20 nm. Red dotted circles border the inorganic core, while green dotted circles indicate the protein shell. Red arrows point to the lattice fringe patterns. (C) Size distribution of the inorganic core, as determined by Image J measurements of the TEM images. (D) XRD patterns and (E) Raman spectroscopy measurements of the nanoparticles.

peaks are all quite sharp, indicating a relatively high level of crystallinity.

The presence of the $ZnFe_2O_4$ phase is also confirmed by the Raman analysis (Fig. 1E); indeed, the most characteristic peaks at about 319, 460 and 650 cm^{-1} are present. They belong to the F2 g(2), F2 g(3) and A1 g modes, respectively.[33,34]

Analysis of the hydrodynamic diameter of the nanoparticles by photon correlation spectroscopy (more commonly known as DLS analysis) revealed average dimensions above 150 nm (see Table 1 and Fig. 2). Pictures of the nanoparticle solutions (Fig. S1C) show optimal stability of the samples even after 2 months of storage at 4 °C.

When MNPs were loaded with *cis*Pt, a slight increase in the average diameter was observed (Table 2). These values were higher than those expected considering the dimensions of the inorganic core, probably because of the swelling of the protein shell and interparticle interactions between the protein coatings. However, this did not affect the stability of the nanoparticle solutions, which remained clear and did not show any sign of aggregation. The low PDI values, always below 0.2, also confirmed this assumption, indicating a homogeneous distribution of particle sizes. The surface charge of MNP@BSA was negative at each step with values around −11 mV. The hydrodynamic size of the particles was monitored over time for up to one week both in PBS and in cell culture medium (with or without 10% FBS). As shown in Fig. 2B, while the size in PBS remained unchanged, when MNP@BSA were dispersed in serum-added cell medium, the size gradually increased from approximately 150–217 nm after 24 h up to around 400 nm after 7 days. This increase is due to the adsorption of serum components, as indeed confirmed by pictures of the tubes with the nanoparticles dispersed in 10% FBS medium (Fig. S1D). The dispersion looks clear without any aggregates. On the other hand, when the particles were dispersed in the cell medium without serum, the size increase recorded by DLS was significant, with measurements reaching 1 μm after one week; moreover, pictures of the solution show the progressive aggregation and precipitation of the nanoparticles.

Further characterization by gel electrophoresis and Coomassie staining confirmed the successful functionalization

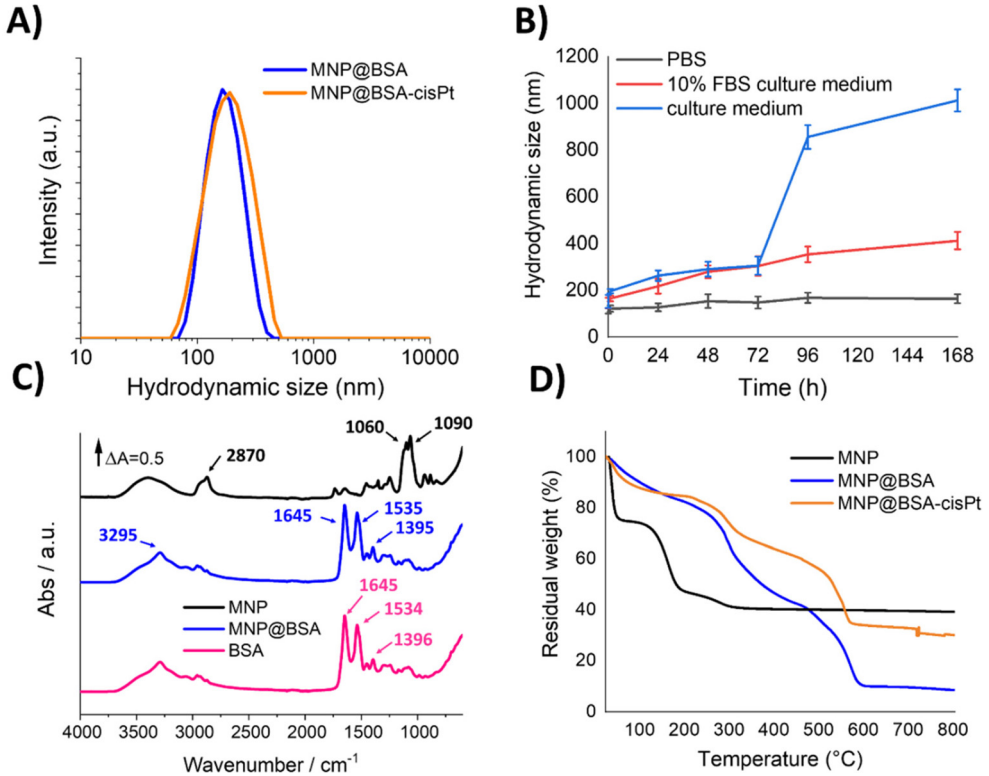

Fig. 2 (A) Hydrodynamic size of MNP@BSA in aqueous solution, as determined by DLS measurements. (B) Size distribution of MNP@BSA over time dissolved in PBS or cell medium (with and without 10% serum), as determined by DLS measurements. (C) FTIR measurements of the MNP after synthesis (black curve) and after BSA functionalization (blue curve), and of BSA (fuchsia curve). (D) TGA curve of the nanoparticles during each step of preparation: after the synthesis (black curve), after BSA coating (blue curve) and after *cis*Pt loading (orange curve).

of the nanoparticles with BSA and the subsequent adsorption of different quantities of *cis*Pt (Fig. S2). While MNP@BSA showed a well-defined migration band, this tended to broaden as increasing quantities of *cis*Pt were added, until it was almost completely retained in the well when the highest amount of drug was used (Fig. S2B). The presence of the organic shell was evidenced by Coomassie blue staining of the gel (Fig. S2A, right band). Remarkably, when HSA was used instead of BSA, MNP functionalization was effective as well. In fact, the protein shell was clearly detected upon gel staining, with the band showing similar features to that of BSA (Fig. S2A, left band). These data further validate our protocol; however, as stated previously, bovine albumin was used throughout the study due to the high HSA cost.

The gel in Fig. S2C shows the migration pattern of the nanoparticles maintained at 37 °C and 5% CO_2 in complete cell medium at predetermined times (1, 24, 48, 96 and 168 h). The pattern confirmed the DLS data, as indeed the nanoparticles partially remained stuck in the deposition well and did not display a narrow migration band, likely due to the adsorption of serum proteins.

The chemical groups on the surface of the MNPs at each step of functionalization were analyzed using FTIR spectroscopy. After the synthesis (Fig. 2C, black curve), the presence of chemical groups belonging to the solvent (tetraethylene glycol) could be observed, such as the peaks at 1060 and 1090 cm^{-1}, typical stretching of the C–O bonds, and that at 2870 cm^{-1} attributed to the stretching of the CH_2 bonds.

When the surface of MNPs was functionalized with BSA, the FTIR spectrum (Fig. 2C, blue curve) was comparable to that of the free protein (Fig. 2C, fuchsia curve). In fact, the IR peak at 3295 cm^{-1} could be assigned to the stretching vibration of the –OH groups, while the peak at 1645 cm^{-1} was typical of the stretching of C═O groups of the amides and that at 1535 cm^{-1} of the stretching of the C–N group and bending of the N–H groups, respectively. Finally, the signal at 1395 cm^{-1} was generally due to the free carboxyl groups of the side chains.

Thermogravimetric analysis was performed to assess the thermal stability and degradation of the MNPs, MNP@BSA, and MNP@BSA-*cis*Pt, as shown in Fig. 2D. Additionally, the first derivatives of the three curves were calculated to better appreciate the degradation kinetics as a function of temperature (Fig. S3A), and the differential thermal analysis (DTA) curves were analyzed to show the energy change associated with each phase of weight loss (Fig. S3B).

As can be seen, thermal decomposition of the samples occurred in multiple stages throughout the entire temperature range (0–800 °C) analyzed. Typically, the initial decomposition could be associated with the primary thermal degradation of more unstable compounds, while subsequent ones could be

due to the thermal degradation of more thermally stable species and/or the compact matrix.[35]

For the as-synthesized MNPs, all weight loss occurred at T < 350 °C, but it happened in several steps (Fig. 2D, black line). The first loss of about 20% was observed at T < 100 °C and was attributable to the evaporation of either adsorbed or incorporated water. The intensity of this event depends on the amount of water present in the sample. This was confirmed by the DTA curves, which showed an endothermic peak, in agreement with the literature.[36] Subsequently, two more steps were registered, at 100 < T < 200 °C and 200 < T < 350 °C, with losses of approximately 25% and 5%, respectively. These weight losses correspond to the degradation of residual organic matter remaining after the synthesis of the MNPs, including traces of the solvent and surfactant (acetone, ethanol, and tetraethylene glycol) used in the synthesis. Analysis of the DTA curves in Fig. S3B shows that the associated exothermic energy is not particularly high, suggesting that the organic residues are probably already partially degraded and not much energy is needed for their complete degradation. No further changes were observed at higher temperatures; in fact, the $ZnFe_2O_4$ inorganic material proved to be thermally stable over the temperature range studied and neither phase changes nor degradation occurred. A residual weight of about 40% was recorded at T > 350 °C, which represented the amount of the inorganic domain of the NPs.

On the other hand, the TGA curve of MNP@BSA was different (Fig. 2D, blue line). In fact, the weight loss associated with water desorption was much smaller (about 10%); this difference could be explained by considering that MNP@BSA were lyophilized and, therefore, the amount of residual water still present was lower than that for the unmodified MNPs, which were just dried at 40 °C. A significant loss was observed for 300 < T < 600 °C, which clearly corresponded to the degradation of BSA. This protein, with its more complex three-dimensional structure, is more thermally stable and requires more energy (*i.e.*, higher temperatures) for its degradation in comparison with the smaller molecules of solvent and surfactant. Such degradation occurs with a significant release of energy, as seen in the intense exothermic peak observed in the DTA curve. The residual weight of MNP@BSA at 800 °C is about 8%, much lower than the MNP sample, indicating that the proportion of $ZnFe_2O_4$ is much smaller in this sample. This is reasonable considering the presence of high molecular weight BSA. For MNP@BSA-*cis*Pt, on the other hand, the TGA profile does not change significantly, and the same qualitative steps observed for MNP@BSA are also recorded for MNP@BSA-*cis*Pt (Fig. 2D, orange line). The main difference is the higher residual weight at 800 °C, which is about 35% and due to the high atomic number of Pt, stable at high temperatures. Nevertheless, the position of the peaks indicating the degradation of BSA shifted to slightly lower temperatures by about 15–20 °C, suggesting that the intercalation of *cis*Pt molecules led to a small decrease in the thermal stability of the protein, maybe caused by slight changes in its tridimensional conformation.[37]

3.3 Magnetic characterization

Fig. 3A shows the magnetization curves for the MNPs before and after BSA functionalization. The MNPs are superparamagnetic due to their small size (about 7 nm), which is below the single domain size; therefore, they display zero coercivity and remanent magnetization. The magnetization of the MNP samples was measured at room temperature as a function of the magnetic field up to 1 T. The as-prepared MNPs showed higher saturation magnetization (about 71 emu g^{-1}) than those with the BSA shell, for which the value dropped to 54 emu g^{-1}. This reduction may be due to the water transfer procedure and surface coating with the BSA molecules.[38] These values are in accordance with previous studies that analyzed the magnetic properties of $ZnFe_2O_4$ nanoparticles with the same size of magnetic domain.[28,39,40]

MNP@BSA were evaluated using MRI to determine their behavior as contrast agents. At 1 T, the T_2 contrast was quite intense, with an r_2 of 133 s^{-1} mM^{-1}, which was in line with other reported magnetic nanoparticle preparations. Therefore, the BSA coating did not interfere with the ability to generate T_2-weighted images and promoted a non-negligible T_1 contrast, with an r_1 of 8.2 s^{-1} mM^{-1}. The r_2/r_1 ratio is 16.2, which favors MNP@BSA as agents for T_2 imaging, but, with appropriate sequences, it could be possible to use these nanoparticles in dual-contrast imaging protocols.

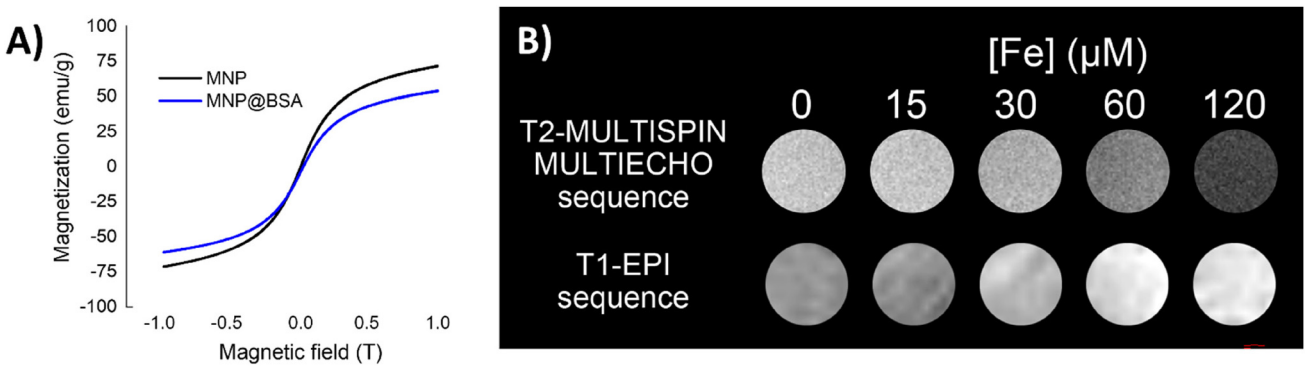

Fig. 3 (A) Magnetization curves for MNPs with (blue curve) and without (black curve) the BSA shell. (B) MR measurements of MNP@BSA in agarose phantoms analyzed at 1 T with a T_2-MSME sequence (TR: 3000 ms, TE: 77 ms) and a T_1-EPI sequence (TR: 2000 ms, TE: 16 ms, TI: 37 ms).

3.4. Loading of *cis*Pt

To determine the amount of encapsulated drug, and therefore the encapsulation efficiency of MNP@BSA, the ratio between the moles of Pt detected by elemental analysis and the moles of Pt added during the preparation of MNPs was calculated, as reported in Table 3.

By increasing the initial concentration of *cis*Pt (from 1.5 to 6 μmol, see the first column of Table 3) in the functionalization mixture, the encapsulation efficiency (%EE) decreased from about 74% to 50%, respectively (second column of Table 3). Notably, by increasing the feeding concentration of the drug, the amount of *cis*Pt loaded into the protein shell increased (fourth column of Table 3) but the corresponding loading ratio (%LR) shifted from 35% to about 18%.

Reports in the literature indicate that HSA can bind around 5 molecules of *cis*Pt[41] and crystallographic data provide evidence that cisplatin preferentially coordinates to His and Met side chain residues located on the protein surface.[37] In the case of BSA, a recent study estimated only one binding site for cisplatin using the Stern–Volmer equation.[42] In our study, the final *cis*Pt/MNP@BSA molar ratio ranged from 25 to 40. From the BCA assay and elemental analysis, it was determined that approximately 5 BSA molecules were linked per MNP; thus, each BSA molecule should bind about 5–10 *cis*Pt molecules. This range of drug molecules per protein unit exceeds the expected value, but it is likely that *cis*Pt interacts with the surface of the magnetic nanoparticles.

In an attempt to increase the amount of *cis*Pt loaded, the nanoparticles were crosslinked with 0.025% glutaraldehyde, as reported elsewhere.[43] In detail, three glutaraldehyde/BSA ratios were tested, *i.e.* 1.5, 3.0, and 4.5 μg of aldehyde per mg of protein. However, despite BSA cross-linking, the encapsulation efficiency of cisplatin did not improve, reaching a maximum of approximately 43% when 6 μmol of cisplatin were used. In addition, the use of glutaraldehyde negatively impacted the colloidal stability of the nanoparticles. Based on these findings, MNP@BSA used in subsequent cellular studies were prepared without the cross-linking step.

3.5. Cellular studies

3.5.1. 2D cellular assays. Cellular studies were performed using breast cancer cells, the phenotype of which was previously studied and characterized by our group.[44]

Table 3 Encapsulation efficiency (%) of *cis*Pt, molar ratio of *cis*Pt/MNP@BSA and drug loading ratio (%). The loading ratio (%) was estimated as the percentage ratio of the final molar ratio (fourth column) to the initial *cis*Pt/MNP molar ratio (third column)

*cis*Pt added (μmol)	Encapsulation efficiency (%)	*cis*Pt/MNP@BSA ratio		Loading ratio (%)
		Initial	Final	
1.5	73.8 ± 4.1	67	23 ± 5	34.6 ± 7.9
3.0	61.1 ± 4.8	133	29 ± 1	21.8 ± 1.0
6.0	49.7 ± 3.7	267	49 ± 4	18.3 ± 1.4

First, 2D cell viability assays were performed using two breast cancer cell lines, MCF-7 and MDA-MB-231. MTT and Trypan Blue exclusion assays were conducted by incubating the cells with three concentrations of MNP@BSA (30, 60 and 120 μg mL^{-1} referring to the inorganic domain). These concentrations correspond to about 290, 580 and 1160 μg mL^{-1} of BSA. Three time points (24, 72 and 120 h) were used as incubation times. The results of the two assays (Figs. S4 and S5) show the good biocompatibility of MNP@BSA. Indeed, in the MTT assay, the percentage viability for cells incubated with 30 and 60 μg mL^{-1} nanoparticles was higher than 80%. When the MDA-MB-231 cells were exposed at the highest concentration for 5 days, the viability reached 79 ± 9%, while it remained over 80% at the other two concentrations. For MCF-7 cells incubated with the nanoparticles for 5 days, the viability was between 72% at the highest concentration and 79% (at the lowest).

In the Trypan Blue assay, viability was reported as the number of live cells over the total cell counts. The cells showed a slightly lower viability percentage at the longest incubation time and at the highest concentration with values close to 68% and 67% for MCF-7 and MDA-MB-231, respectively. The general trend, consistent with the MTT assay, is of good biocompatibility in both cell lines.

The internalization of the nanoparticles was evidenced by ultrastructural analysis of the cells incubated with MNP@BSA, as reported in Fig. S6. The images show the nanoparticles approaching the cell membrane (Fig. S6A and B) and then their compartmentalization in the endosomes (Fig. S6C and D) after 1 and 24 h of incubation, respectively. When the cells were kept in the culture for additional time up to 7 and 15 days, the progressive degradation of the nanoparticles was observed. Indeed, after 7 days of incubation, some nanoparticles were still visible and localized in the endosomes but others underwent degradation in the lysosomes (Fig. S6E and F). Finally, after 15 days of incubation, they were almost completely degraded, as shown in Fig. S6G and H.

3.5.2. Internalization of MNP@BSA in 3D tumor models. To test the ability of MNP@BSA to cross biological barriers, their internalization in 3D breast tumor models was studied. To track the fate and distribution of the nanoparticles, they were made fluorescent by conjugating rhodamine 101 to the BSA shell. The fluorophore conjugation procedure is described in detail in the SI. Fig. S7 reports the characterization of fluorescent nanoparticles.

3D breast tumor models were prepared using MCF-7 cells, which, based on our previous findings, formed more uniform and stable 3D structures compared to MDA-MB-231 cells.[29]

Two different cell culture approaches were followed. In the first approach, tumor mammospheres were kept in suspension, and the interaction between the mammospheres and the nanoparticles was investigated under these conditions.

After MCF-7 mammospheres were prepared and grown in suspension for 5 days, rhodamine 101-labelled MNP@BSA (MNP@BSA-Rhod101) were added to the culture medium. The mammospheres were collected, fixed, and imaged under a con-

focal microscope after either 24, 48 or 72 h of incubation. Fig. 4A–C″ shows the internalization of the nanoparticles within the spheroids. After 24 and 48 h (Fig. 4A–A″ and B–B″, respectively) the fluorescence was typically point-like due to the accumulation of nanoparticles within the endosomal compartment. After 3 days (Fig. 4C), the signal became more diffuse inside the cells, which was likely due to the degradation of the protein shell by lysosomal enzymes, and consequent release of the fluorophore.

The viability of the mammospheres after incubation with the nanoparticles was estimated using the live/dead assay. The trend shown in the histograms of Fig. 4F provide evidence of the optimal viability of the nanoparticles compared to control mammospheres after 24, 48, and 72 h of incubation. The images in Fig. 4D and E present the results of the live/dead assay on mammospheres after 24 h. Fig. S8 shows images from the same assay after 48 and 72 h of incubation with the nanoparticles. At all time points, the green calcein channel, corresponding to live cells, shows strong fluorescence, while the red signal associated with dead cells is not detectable in any of the samples, neither the control nor the treated mammospheres.

In the second approach, hydrogel-embedded tumor spheroids were prepared by growing MCF-7 cells in 0.19% agarose hydrogel. The formation of multicellular spheroids was monitored over time before proceeding with the MNP internalization studies. As shown in Fig. S9, the MCF-7 cells formed almost regularly shaped spheroids with an average diameter of approximately 100 μm after 12 days.

To evaluate the ability of MNP@BSA to be internalized by spheroids and cross the hydrogel, which simulated the extracellular matrix, rhodamine 101-labelled MNP@BSA were incubated with the spheroids before studying their internalization by fluorescence microscopy. Fig. S9B and C clearly show the presence of the fluorescent signal after 6 h and up to 24 h. To confirm the internalization of the MNPs in the spheroids, ultrastructural analysis was carried out. For this purpose, the spheroids were recovered from the hydrogel after treatment with β-agarase from *Pseudomonas atlantica* at 37 °C overnight. Subsequently, the samples were processed for electron microscopy. Fig. S9D–F shows images of spheroid cells that have internalized the nanoparticles in the endosomes, as indicated by the red arrows.

These data thus highlight, on one hand, that MNP@BSA are able to penetrate through the hydrogel matrix and, on the other hand, that they can be internalized by the cells of the spheroids.

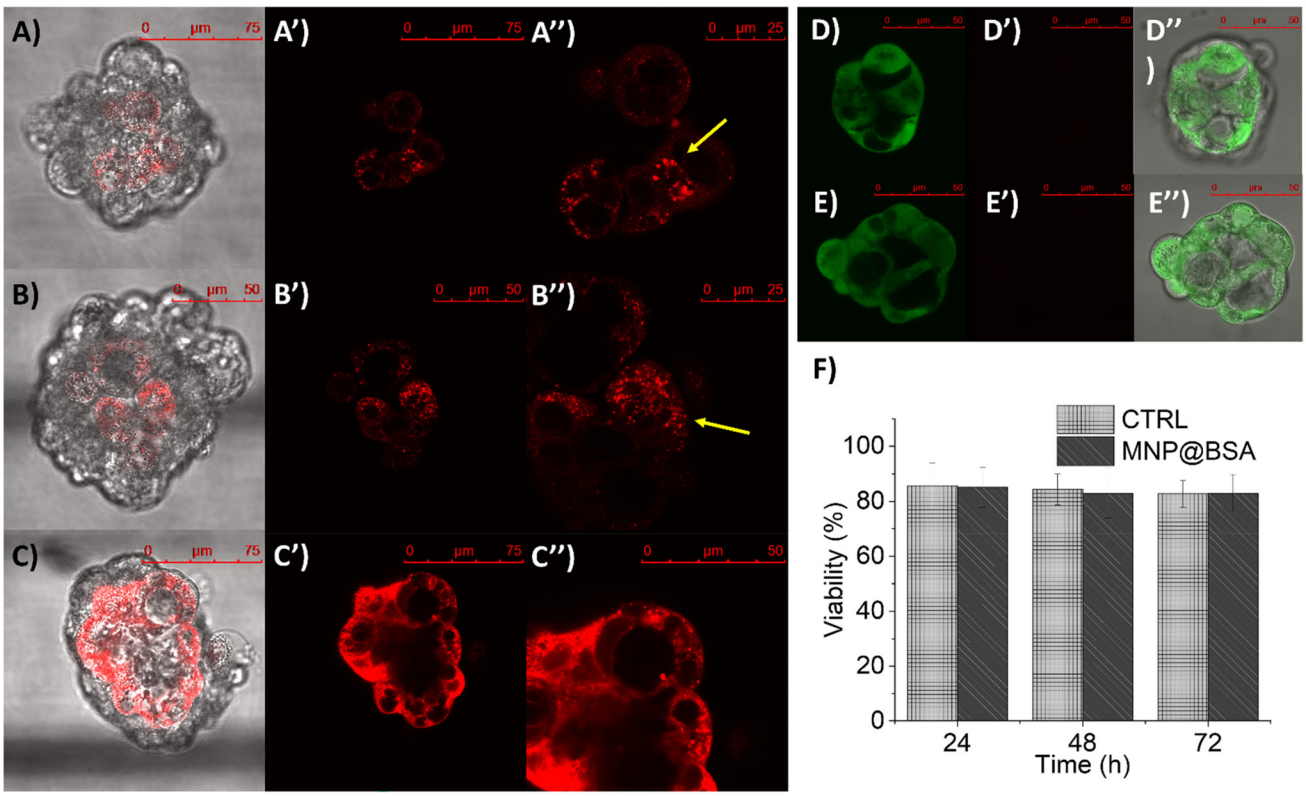

Fig. 4 (A–C) Confocal microscopy images of the MCF-7 spheroids incubated with MNP@BSA-Rhod101 for 24, 48 and 72 h. The images show the merged bright field and fluorescent channels. (A′–C′) Fluorescent channels. (A″–C″) Higher magnification insets of (A′–C′). (D–D″) Confocal microscopy images of the mammospheres from the live/dead assay performed after 24 h incubation with MNP@BSA; (E–E″) Corresponding control mammospheres (without MNP@BSA). (D and E) The calcein channel; (D′–E′) the propidium homodimer channel; (D″–E″) the merged fluorescent channels and the bright field. (F) Cell viability of the mammospheres after incubation with MNP@BSA for 24, 48 and 72 h. Viability was estimated by quantifying the fluorescence signals from the live/dead assay.

3.5.3. MNP@BSA-mediated transport of cisplatin to mammospheres. The ability of the MNPs to transport *cis*Pt inside cellular spheroids was also tested on both mammospheres grown in suspension and on those embedded in agarose hydrogel; these two studies are qualitative in nature and are not intended to provide a complete analysis of the interactions and effects of the drug on 3D cell cultures.

The mammospheres in suspension were incubated with MNP@BSA, MNP@BSA-*cis*Pt or free *cis*Pt (200 nM NP concentration, corresponding to about 10 μM Pt) for 24 h before being processed using the CellTiter-Glo® 3D cell viability assay. This concentration was chosen based on recently published studies that analyzed the drug response of spheroids embedded in hydrogels.[45,46] The results of the luminescence assay, which measured the amount of ATP in metabolically active cells, were normalized to the amount of protein and showed a significant reduction in ATP content in all the treated samples (Fig. S10A). In detail, the data indicate that spheroids incubated with MNP@BSA-*cis*Pt exhibit a remarkable reduction in cell viability compared to those incubated with the same amount of free *cis*Pt and nanoparticles. The optical images in Fig. S10B and C confirm that, upon treatment with MNP@BSA-*cis*Pt, the spheroids appear to be damaged with multiple detached and dying cells, while control samples appear more regular and viable.

The same experiment was performed on hydrogel-embedded mammospheres. After 12 days of growth, the spheroids were incubated with *cis*Pt-loaded MNP@BSA (at a concentration of 200 nM, corresponding to about 10 μM of Pt), free drug, or MNP@BSA. After 24 h of incubation, a live/dead assay was performed to evaluate the effects of the treatment on spheroid viability. Fig. 5 presents fluorescence images of the spheroids and quantitative data obtained from plate reader measurements. A comparative analysis of the images shows the morphology of the spheroids and the distribution of green and red fluorescence signals. While control spheroids and those incubated with MNP@BSA display a regular rounded shape and a predominance of green fluorescence (associated with calcein, which is metabolized in viable cells) over the red signal (associated with ethidium homodimer, which is permeable to dead cells), the mammospheres treated with either free or *cis*Pt-loaded MNP@BSA lose their integrity, show an irregular structure with detaching, dying cells and a predominance of red fluorescence over the green one. Quantitative analysis confirms this trend and shows a significant difference in the ratio of dead to live cells in the samples exposed to *cis*Pt compared to the control. In detail, the intensity of the calcein signal of the spheroids treated with either MNP@BSA-*cis*Pt or *cis*-Pt is about 10 and 5 times lower than that of control cells, respectively. On the other hand, quantitative data related to ethidium homodimer indicate a 2-fold and 2.8-fold intensity increase in the case of tumor spheroids treated with either *cis*-Pt or MNP@BSA-*cis*Pt compared to control spheroids.

In a previous study, we showed the capacity of free *cis*Pt to enter the hydrogel matrix and reach the 3D tumors. In the present study, *cis*Pt was successfully delivered by magnetic nanoparticles to both suspended mammospheres and hydrogel-embedded breast tumor spheroids. Though the data presented are merely qualitative, they indicate that this system can be used to study nanoparticle-mediated drug transport and drug response mechanisms.

3.5.4. Analysis of MNP@BSA translocation through an enterocyte-like monolayer. To assess the ability of MNP@BSA to transit through an epithelial barrier, a simplified model of the intestinal epithelium was developed by growing Caco-2 cells on transwell membranes, as depicted in the sketch in Fig. 6A.[47] Cells were continuously grown for up to 21 days post seeding (dps), to obtain a tight monolayer of spontaneously differentiated enterocyte-like cells. Upon establishment of the mature monolayer, rhodamine 101-labelled nanoparticles were added to the apical chamber of the transwell (henceforth reported as UP chamber for simplicity) that were left to incubate for the set time points (1, 3, 5 and 7 days). Then, the media of the UP and basolateral chambers (henceforth reported as DOWN chamber for simplicity) were collected and analyzed by fluorescence measurements and ICP-AES. Different transwells were prepared in parallel for each time point. The same assay was also performed without the cell monolayer to compare the free diffusion kinetics of the nanoparticles through the transwell membrane with cell-mediated transport from the apical to the basolateral compartment.

The curves in Fig. 6B and C show the fluorescence signal measurements recorded over time in both compartments, with (black curves) or without Caco-2 monolayers (grey curves). As expected, diffusion through the transwell membrane was faster without the cells, with a rapid fluorescence decrease in the upper chamber and a corresponding increase in the lower chamber after 1 day. The system appeared to reach a diffusive equilibrium after 3 days. On the other hand, in the presence of the cell monolayer (black curves), transport from the apical to the basolateral side was slower and exhibited a linear trend over time in both chambers. Based on these findings, the apparent permeability (Papp) and the percentage recovery were estimated. The Papp is equal to 5.5 ($\pm$0.7) $\times$ 10^{-7} cm s^{-1}, while the % recovery is around 82 $\pm$ 3%. Interestingly, Fig. 6D shows the variation of Fe content over time, measured in the culture medium recovered from the UP and DOWN chambers, and in the cellular monolayer. Reasonably, the Fe amount diminished in the UP chamber while increasing in the DOWN chamber over time. The Fe content measured in the cells showed three different steps: a fast linear increase from time 0 to 3 days, followed by a steady state from day 3 to 5 days, and finally a slower increase up to 7 days. This trend shows that apical-to-basolateral transport through the epithelial-like monolayer is not a continuous process but involves multiple steps and mechanisms. These include an initial phase of fast internalization followed by a plateau where internalization is balanced by release toward the basolateral side, and finally a further slight acceleration of nanoparticle entry.

Finally, the images in Fig. 6E and F show the Caco2 monolayer upon incubation with the nanoparticles for 5 days. The bright field image shows the tightness of the mono-

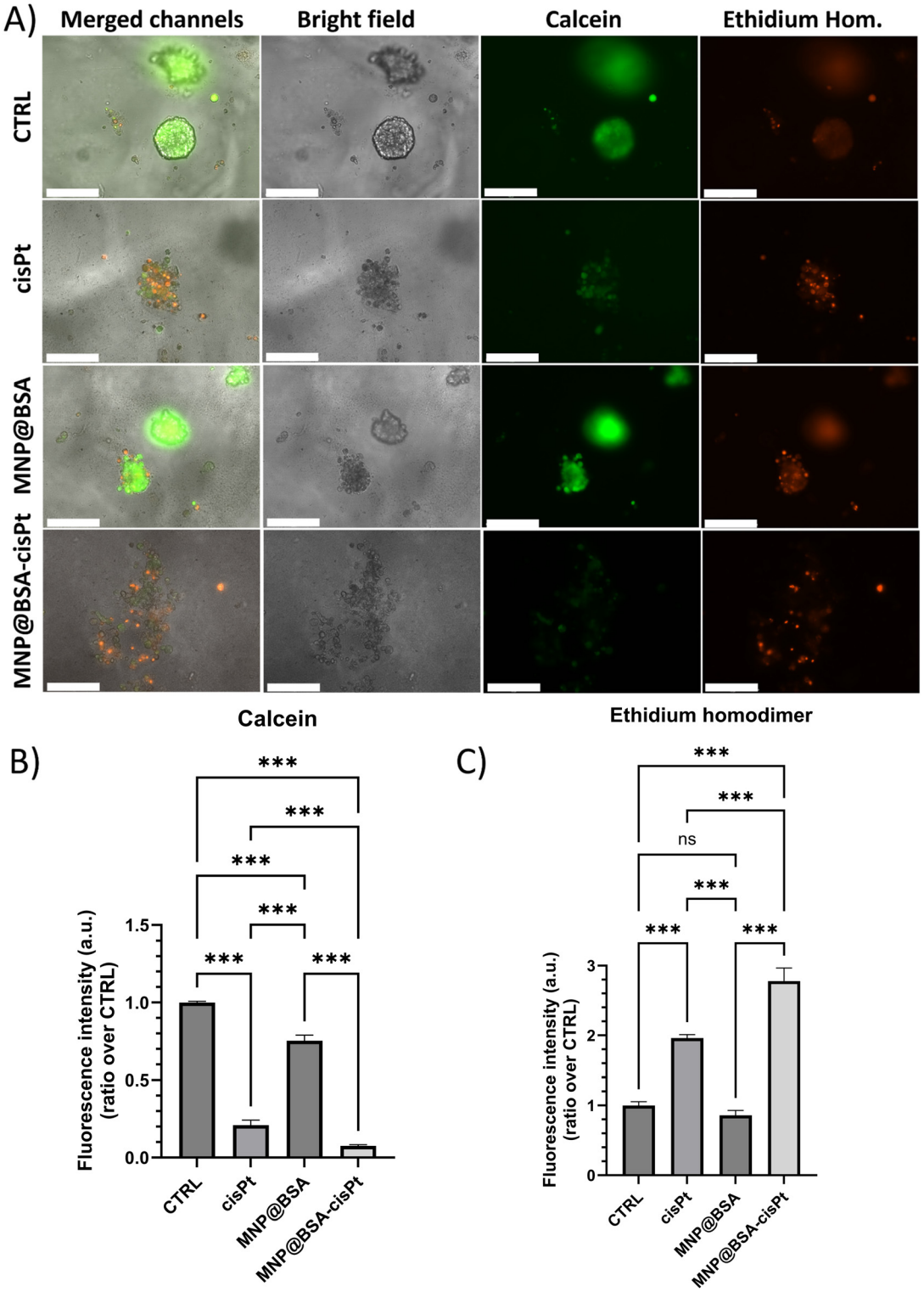

Fig. 5 (A) Live/dead assay performed on MCF-7 spheroids embedded in the hydrogel after incubation for 24 h with MNP@BSA, MNP@BSA-*cis*Pt, and free *cis*Pt. (B) Average fluorescence intensity from calcein (live cells); (C) average fluorescence intensity from ethidium homodimer (dead cells). Statistical significance is shown as $*p < 0.05$, using one-way analysis of variance.

layer built by Caco-2 cells on the transwell membrane, while the fluorescent image reports the distribution of nanoparticles. Beyond a general red background in almost all cells, some large spots, likely associated with clustered particles inside the cells, are visible. Cell nuclei were stained with DAPI but were not all visible due to the different focus on the *Z*-axis.

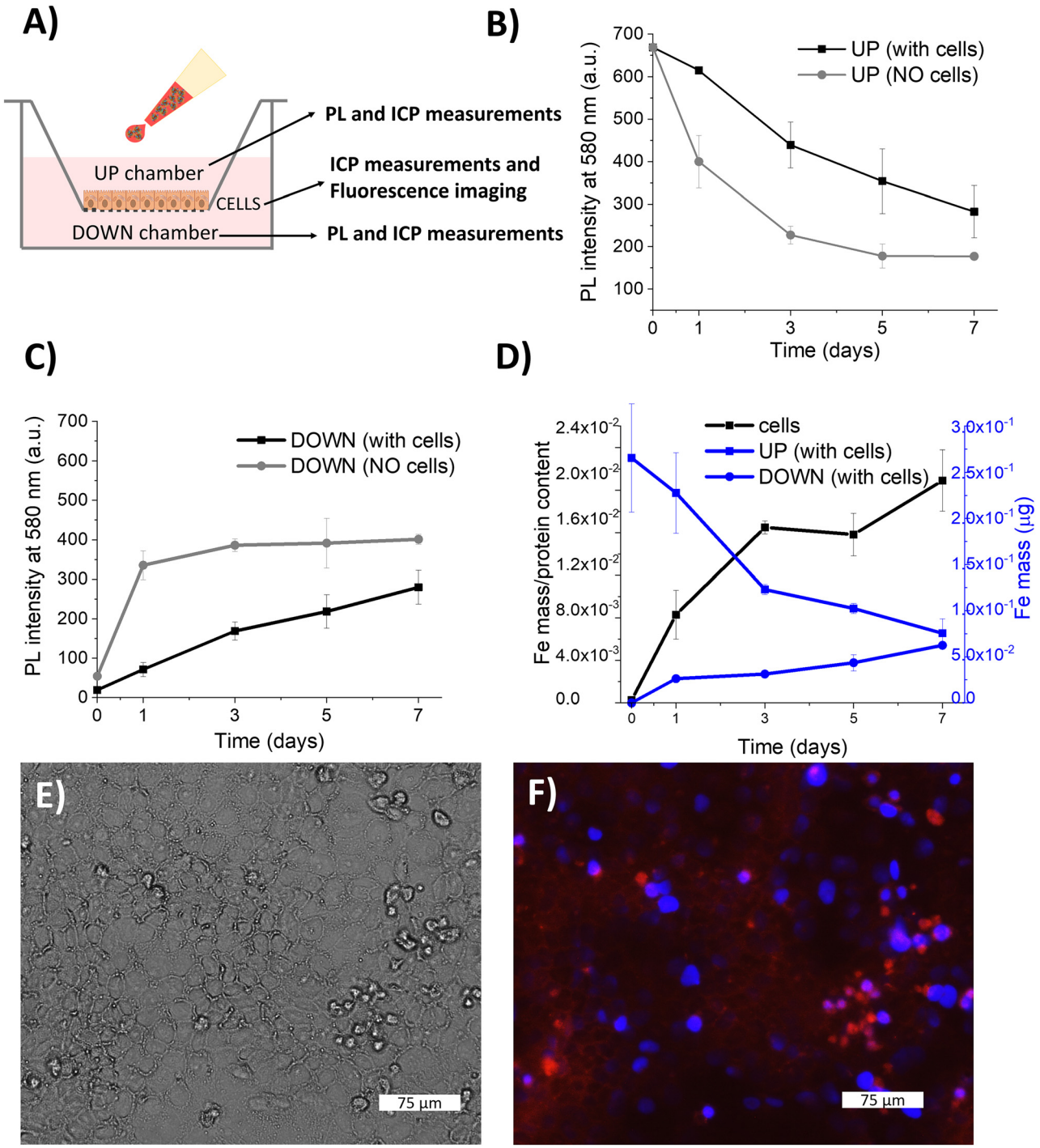

Fig. 6 (A) Sketch of the experiment setup used to assess MNP@BSA delivery through an intestinal epithelium barrier. (B and C) Fluorescence intensity measurements of MNP@BSA-Rhod101 in the UP and DOWN chambers of the transwell, respectively, over a 7 day period. The experiments were performed both with and without the Caco2 monolayer. (D) Estimation of the Fe content by elemental analysis in the upper and lower chambers of the transwell and in the Caco2 monolayer after incubation with MNP@BSA-Rhod101 over time for up to 7 days. Bright-field (E) and fluorescent (F) optical microscopy images of the Caco-2 monolayer after 5 days of incubation with MNP@BSA-Rhod101. Cell nuclei were stained with DAPI. Scale bars correspond to 75 µm.

Other images at lower magnification are presented in Fig. S11, which include both control samples (without nanoparticles) and Caco-2 cells after 5 days of incubation with MNP@BSA-Rhod101.

4. Discussion

In this work, zinc ferrite magnetic nanoparticles of approximately 7 nm in size were synthesized by thermal decompo-

sition of organometallic precursors (Scheme 1). Fe and Zn are metals naturally present in the human body, where they perform multiple functions, including enzyme synthesis, oxygen transport, *etc*.[48,49] and have systems for their absorption, transport, use, and disposal (although for iron, being particularly relevant, excretion is minimal).[50] In the case of zinc, there is a tolerance range of daily intake of up to 15 mg in adults.[51] These aspects, together with biocompatibility and biodegradation, are of fundamental importance for the safe use of inorganic materials.[52]

Biodegradation implies that the nanoparticles undergo dissolution over time with the consequent recycling or disposal of the constituent elements (in this case, Fe and Zn). To date, numerous studies reported in the literature demonstrated the biodegradability of iron oxide nanoparticles.[53,54] These studies show that, in addition to the inorganic core, the organic coating plays a crucial role in regulating the modes of and times required for degradation of the nanoparticles.

Among the various procedures developed for making inorganic nanoparticles soluble in an aqueous environment while preserving the chemical and physical properties of the inorganic material, those based on the use of natural polymers or biomolecules are certainly preferable. These methods significantly reduce potential risks related to toxicity and immunogenicity of the NPs, especially if their application is extended to *in vivo* tests.[55–58]

Therefore, BSA represents an optimal surface ligand due to its excellent stability and natural role as a transport molecule. In this study we demonstrate the use of albumin as a biocompatible organic coating for the surface functionalization of $ZnFe_2O_4$ nanoparticles.

BSA was readily adsorbed onto the MNPs through a variety of non-covalent interactions between the protein residues and the metallic surface; indeed, carboxylate groups from BSA (Asp, Glu residues) could coordinate Fe^{3+}/Fe^{2+} ions on the MNP surface, and surface hydroxyl groups on magnetic nanoparticles could form hydrogen bonds with amide groups, hydroxyl groups and carboxyl groups of BSA. The resulting MNP@BSA were stable over time under physiological conditions. The average amount of BSA molecules per MNP, as estimated by elemental analysis and protein quantification assays, was found to be about 5.5. Since the average dimension of albumin[59] is about 3.5 nm, it is expected that a single nanoparticle coated with 6 molecules of albumin would have an overall diameter of approximately 27 nm. However, the dimensions measured by photon correlation spectroscopy were much bigger, with a hydrodynamic diameter of approximately 180 nm. Considering the high colloidal stability of the particles, even in complex media such as serum-added cell culture medium, this discrepancy is probably due to interparticle interactions between the protein shells of adjacent particles. Nevertheless, the nanoparticle solutions appeared to be clear without any aggregates (Fig. S1), as confirmed by the electrophoretic migration pattern of the nanoparticles (Fig. S2). The presence of BSA stabilizes the nanoparticles but cannot prevent interaction with blood proteins, contributing to the formation of the protein corona.[60] It is likely that the BSA coating acts as an artificial protein corona that delays adsorption of other plasma proteins and reduces opsonin binding, thus prolonging the circulation time of the nanoparticles and of the drugs.[61] According to the literature, the BSA coating is not a replacement for protein corona formation, but a modulator, and the final biological behavior might depend on how BSA interacts with other proteins.[62]

Furthermore, the free chemical groups on the protein shell provide anchoring sites for the conjugation of biomolecules or fluorophores. In this study, the nanoparticles were fluorescently labelled with rhodamine 101, making them traceable inside cells.

The presence of the BSA shell slightly affected the magnetic properties of the nanoparticles, as evidenced by the *MH* curves at 300 K. Indeed, the saturation magnetization of MNP@BSA (54 emu g^{-1}) was lower than that of pristine $ZnFe_2O_4$ nanoparticles (71 emu g^{-1}). Nevertheless, magnetic resonance measurements at 1 T showed that MNP@BSA could be used as agents for T_2 imaging, displaying a r_2/r_1 ratio equal to 16.2, which was comparable to that of previously published data.[63]

To show the delivery potential of MNP@BSA, chemotherapeutic *cis*Pt was incorporated into the albumin shell. Different amounts of *cis*Pt (75, 150 or 300 μL, 20 mM) were used and the highest %LR and %EE (around 35% and 74%, respectively) were reached using the lowest feeding amount of *cis*Pt, as determined by elemental analysis.

Upon completion of the physico-chemical characterization, their interaction with cellular models was investigated at different levels. First, the cytocompatibility of MNP@BSA was assessed in 2D and 3D cell models of breast cancer, showing good biocompatibility for up to 3 days of incubation and 120 μg mL^{-1} administration.

Furthermore, ultrastructural analysis of the cells incubated with MNP@BSA showed that the nanoparticles could be degraded in the cell lysosomes over time. Indeed, after initial internalization and localization of the nanoparticles in the endosomes, they underwent degradation, and the process was almost completed after 15 days of incubation, supporting the hypothesis that the biological nature of the surface coating contributed to accelerating the degradation of the magnetic core.[64,65]

Then, additional studies were performed to investigate the capacity of the nanostructure to penetrate a hydrogel matrix and release the loaded drug into the hydrogel-embedded 3D tumor model. These systems mimic the tumor environment more closely and offer the opportunity to study cell–cell and cell–matrix interactions in addition to other processes, like tumor cell invasion, angiogenesis, and drug penetration.[66,67]

Towards this aim, mammospheres grown in an agarose hydrogel were used as a 3D model to assess the ability of MNP@BSA to penetrate the hydrogel, be internalized by the tumor spheroid cells, and release *cis*Pt. Fluorescent imaging of the hydrogel-embedded spheroids incubated with fluorescent MNP@BSA allowed us to detect the nanoparticles, confirming successful take up (Fig. S9A). Then, the drug transport and

delivery potential of *cis*-Pt-loaded MNP@BSA was evaluated. Qualitative and quantitative data collected confirmed the effective delivery and release of the drug, resulting in cell death and partial disintegration of the mammospheres following 24 h of treatment.

Another type of biological barrier encountered by nanoparticles upon administration consists of specialized epithelia, such as the epidermis and the internal epithelial lining. These structures act as defense barriers against the entrance of exogenous compounds and pathogens, allowing regulated transport from one side to the other. However, they also pose a critical challenge in pharmacology.[68,69]

In the case of the gastrointestinal tract, the nanoparticles should overcome the mucus layer and pass through the intestinal epithelial cells to enter the circulation.[70] Enterocytes are the main cells involved in the absorption process, which generally occurs through transcellular transport, while paracellular transport is prevented by the presence of tight junctions, such as claudin and occludin.[70]

In this study, a simplified model of an epithelial barrier made up of a monolayer of Caco-2 cells was used to assess the capacity of MNP@BSA to cross it. Towards this aim, MNP@BSA-Rhod101 were used, and both the fluorescence signal and the amount of Fe in the three compartments of the model (*i.e.*, the apical chamber, the cell monolayer and the basolateral chamber) were recorded over time. The data collected indicate that over time the fluorescence signal and the amount of Fe decrease in the UP chamber and increase in the DOWN chamber. In addition, the multiphasic pattern of intracellular Fe accumulation in the cells is consistent with the variations in Fe content in the upper and lower chambers, thus confirming that there is a progressive internalization of the nanoparticles from the apical side followed by their release in the basolateral compartment over time. Interestingly, an estimation of the Papp of 5.5 (±0.7) × 10^{-7} cm s^{-1} suggests active transport through the epithelial barrier and qualitatively demonstrates the active role of the cellular monolayer in mediating the transepithelial take up of nanoparticles.[71]

5. Conclusions

In this work, magnetic zinc ferrite nanoparticles with an average diameter of 7 nm were prepared and functionalized with a protein coating made of BSA. The resulting MNP@BSA particles were optimally stable under physiological conditions, and their capacity to cross biological barriers and act as a drug carrier was tested. The poorly water-soluble antitumor drug cisplatin was successfully encapsulated in the BSA shell.

Cellular studies with 2D and 3D models of breast cancer were performed to assess the cytocompatibility profile of MNP@BSA. In addition, a hydrogel-embedded 3D model of breast cancer was used to show the ability of the nanoparticles to enter the hydrogel matrix and be internalized in the cell spheroids. Subsequently, the drug delivery efficacy of *cis*Pt-loaded MNP@BSA was evaluated in the hydrogel-embedded 3D tumor spheroids. The results demonstrated the cytotoxic effect of MNP@BSA-*cis*Pt and the cytocompatibility of MNP@BSA.

Moreover, a simplified model of the intestinal epithelium, composed of an apical chamber, a Caco-2 cell monolayer and a basolateral chamber, was used to assess the capacity of the particles to cross a biological barrier. After incubation of fluorophore-labelled MNP@BSA, a progressive decrease in the fluorescence signal and amount of Fe in the apical compartment and an increase in the basolateral compartment were detected accordingly. Thus, the active role of the cellular monolayer in mediating the transepithelial take up of nanoparticles was evidenced.

Overall, the experimental data indicated that BSA was an optimal coating agent for inorganic nanoparticles, as it offered stability in the biological environment, and could be used as a loading platform for lipophilic drugs, allowing for transport through hydrophilic matrices to 3D tumor models and epithelial barriers.

In conclusion, the impact of this work lies in positioning MNP@BSA as a multifunctional theranostic system, supporting the relevance of 3D models for assessing nanoparticle transport and therapeutic efficacy and addressing key translational barriers in nanomedicine.

Author contributions

A. C., A. N., A. M., R. D. C., C. P., C. N. and L. G., investigation and methodology; A. G., A. R., M. D. P., C. P., and A. Q., writing – original draft; G. G., and G. M., resources; A. B., and A. Q., conceptualization and data curation.

Conflicts of interest

There are no conflicts of interest to declare.

Data availability

The data supporting the findings of this study are included in the article and its supplementary information (SI). Supplementary information includes additional TEM images and gel electrophoresis characterization of the MNP@BSA, first derivative curves from TGA measurements and Differential Thermal Analysis, MTT and Trypan Blue viability assays of MCF-7 and MDA-MB-231 cells incubated with the MNP@BSA, TEM images of the MCF-7 cells incubated with the MNP@BSA, a detailed description of the fluorescent labelling of the MNP@BSA with Rhodamine 101, fluorescent and TEM images of breast spheroids incubated with the Rhodamine-labelled MNP@BSA, Cell Titer Glo assay performed with mammospheres incubated with MNP@BSA-cisPt, and additional fluorescent images of the Caco2 cell monolayer incubated with Rhodamine-labelled MNP@BSA. See DOI: https://doi.org/10.1039/d5nr04238k.

Acknowledgements

This work was supported by the Italian Ministry of Research, under the complementary actions of the NRRP "Fit4MedRob – Fit for Medical Robotics" Grant (No. PNC0000007) and Tecnomed Puglia – Tecnopolo per la medicina di precisione (Biotech Lecce Hub) c/o Campus Ecotekne, *via* Monteroni, Lecce, 73100 Italy.

The authors would like to acknowledge the support from Mrs Enrica Stasi and Viviana Rizzello.

References

1 D. Lombardo, M. A. Kiselev and M. T. Caccamo, *J. Nanomater.*, 2019, **2019**, 3702518.
2 M. Li, Q. Tang, H. Wan, G. Zhu, D. Yin, L. Lei and S. Li, *APL Mater.*, 2024, **12**, 100601.
3 A. Quarta, C. Piccirillo, G. Mandriota and R. Di Corato, *Materials*, 2019, **12**, 139.
4 Y. Wu, M. R. K. Ali, K. Chen, N. Fang and M. A. El-Sayed, *Nano Today*, 2019, **24**, 120–140.
5 J. B. Mamani, J. P. Borges, A. M. Rossi and L. F. Gamarra, *Pharmaceutics*, 2023, **15**, 1663.
6 L. Gandarias and D. Faivre, *ChemPlusChem*, 2024, **89**, e202400090.
7 H. Huang, W. Feng, Y. Chen and J. Shi, *Nano Today*, 2020, **35**, 100972.
8 M. Azizi, R. Jahanban-Esfahlan, H. Samadian, M. Hamidi, K. Seidi, A. Dolatshahi-Pirouz, A. A. Yazdi, A. Shavandi, S. Laurent, M. Be Omide Hagh, N. Kasaiyan, H. A. Santos and M.-A. Shahbazi, *Mater. Today Bio*, 2023, **20**, 100672.
9 M. R. Mohammadi, C. Corbo, R. Molinaro and J. R. T. Lakey, *Small*, 2019, **15**, 1902333.
10 M. Ramachandran, Z. Ma, K. Lin, C. De Souza and Y. Li, *Nanoscale Adv.*, 2022, **4**, 4470–4480.
11 X. Shen, D. Pan, Q. Gong, Z. Gu and K. Luo, *Bioact. Mater.*, 2024, **32**, 445–472.
12 J. Jia, Z. Wang, T. Yue, G. Su, C. Teng and B. Yan, *Chem. Res. Toxicol.*, 2020, **33**, 1055–1060.
13 S. Waheed, Z. Li, F. Zhang, A. Chiarini, U. Armato and J. Wu, *J. Nanobiotechnol.*, 2022, **20**, 395.
14 S. Lamichhane and S. Lee, *Arch. Pharmacal Res.*, 2020, **43**, 118–133.
15 D. A. Belinskaia, P. A. Voronina and N. V. Goncharov, *J. Evol. Biochem. Physiol.*, 2021, **57**, 1419–1448.
16 M. Jaremko, L. Jaremko, M. Alghrably, S. Al-Harthi, A. Alshehri, L. Alhudhali, M. Almohaywi and G. Bennici, in *Nanoparticle Drug Delivery - A Comprehensive Overview*, ed. B. Kumar, IntechOpen, Rijeka, 2025, DOI: 10.5772/intechopen.1011323.
17 H. Ji, Z. Zheng, S. Li, X. Xiao, W. Tang, X. Zhang, Q. Guo, Q. He, S. Cai, P. Jiang, H. Wang, L. Li, X. Xiao and L. Wang, *Interdiscip. Med.*, 2024, **2**, e20240010.
18 A. Spada, J. Emami, J. A. Tuszynski and A. Lavasanifar, *Mol. Pharm.*, 2021, **18**, 1862–1894.
19 G. Hartung, G. Stehle, H. r. Sinn, A. Wunder, H. H. Schrenk, S. Heeger, M. Kränzle, L. Edler, E. Frei, H. H. Fiebig, D. L. Heene, W. Maier-Borst and W. Queisser, *Clin. Cancer Res.*, 1999, **5**, 753–759.
20 W.-W. Qi, H.-Y. Yu, H. Guo, J. Lou, Z.-M. Wang, P. Liu, A. Sapin-Minet, P. Maincent, X.-C. Hong, X.-M. Hu and Y.-L. Xiao, *Mol. Pharm.*, 2015, **12**, 675–683.
21 I. Cucinotto, L. Fiorillo, S. Gualtieri, M. Arbitrio, D. Ciliberto, N. Staropoli, A. Grimaldi, A. Luce, P. Tassone, M. Caraglia and P. Tagliaferri, *J. Drug Delivery*, 2013, **2013**, 905091.
22 Y. Tanaka, *Expert Opin. Biol. Ther.*, 2023, **23**, 579–587.
23 A. S. Chubarov, *Magnetochemistry*, 2022, **8**, 13.
24 J. Xie, J. Wang, G. Niu, J. Huang, K. Chen, X. Li and X. Chen, *Chem. Commun.*, 2010, **46**, 433–435.
25 C. G. Hiremath, M. Y. Kariduraganavar and M. B. Hiremath, *Prog. Biomater.*, 2018, **7**, 297–306.
26 H. Huang, D.-P. Yang, M. Liu, X. Wang, Z. Zhang, G. Zhou, W. Liu, Y. Cao, W. J. Zhang and X. Wang, *Int. J. Nanomed.*, 2017, **12**, 2829–2843.
27 N. Jaiswal, N. Mahata and N. Chanda, *Nanoscale*, 2025, **17**, 11191–11220.
28 Y. Lin, W. Yao, Y. Cheng, H. Qian, X. Wang, Y. Ding, W. Wu and X. Jiang, *J. Mater. Chem.*, 2012, **22**, 5684–5693.
29 A. Quarta, N. Gallo, D. Vergara, L. Salvatore, C. Nobile, A. Ragusa and A. Gaballo, *Pharmaceutics*, 2021, **13**, 963.
30 Y. Sambuy, I. De Angelis, G. Ranaldi, M. L. Scarino, A. Stammati and F. Zucco, *Cell Biol. Toxicol.*, 2005, **21**, 1–26.
31 A. Mazzei, M. Cucchiara, L. Mortara, E. Bossi, R. Schiavone, T. Verri, A. Bruno and A. Barca, *Front. Immunol.*, 2025, **16**, 1527007.
32 M. S. Patil, P. D. Sarvalkar, S. R. Mulani, A. D. Sheikh, R. S. Devan and K. K. K. Sharma, *J. Photochem. Photobiol., A*, 2025, **459**, 116001.
33 P. Galinetto, B. Albini, M. Bini and M. C. Mozzati, in *Raman Spectroscopy*, ed. G. M. Do Nascimento, IntechOpen, London, 2018, DOI: 10.5772/intechopen.72864.
34 S. C. Chabattula, B. Patra, P. K. Gupta, K. Govarthanan, S. K. Rayala, D. Chakraborty and R. S. Verma, *Appl. Biochem. Biotechnol.*, 2024, **196**, 1058–1078.
35 S.-M. Lam, J.-C. Sin, H. Zeng, H. Lin, H. Li, Y.-Y. Chai, M.-K. Choong and A. R. Mohamed, *Mater. Sci. Semicond. Process.*, 2021, **123**, 105574.
36 S. H. Hussein-Al-Ali, M. E. El Zowalaty, M. Z. Hussein, M. Ismail, D. Dorniani and T. J. Webster, *Int. J. Nanomed.*, 2014, **9**, 351–362.
37 G. Ferraro, L. Massai, L. Messori and A. Merlino, *Chem. Commun.*, 2015, **51**, 9436–9439.
38 L. Haim, F. Robert, L. Peres, P. Lecante, K. Philippot, R. Poteau, M. Respaud and C. Amiens, *Nanoscale Adv.*, 2021, **3**, 4471–4481.
39 G. Thirupathi and R. Singh, *IEEE Trans. Magn.*, 2012, **48**, 3630–3633.
40 E. C. Mendonça, C. B. R. Jesus, W. S. D. Folly, C. T. Meneses and J. G. S. Duque, *J. Supercond. Novel Magn.*, 2013, **26**, 2329–2331.

41 L. Massai, A. Pratesi, J. Gailer, T. Marzo and L. Messori, *Inorg. Chim. Acta*, 2019, **495**, 118983.
42 Z. Arabpour Shiraz, N. Sohrabi, M. Eslami Moghadam and M. Oftadeh, *Heliyon*, 2023, **9**, e20090.
43 M. Malekizadeh and H. Rafati, *Colloids Surf., A*, 2024, **690**, 133797.
44 A. M. Giudetti, S. De Domenico, A. Ragusa, P. Lunetti, A. Gaballo, J. Franck, P. Simeone, G. Nicolardi, F. De Nuccio, A. Santino, L. Capobianco, P. Lanuti, I. Fournier, M. Salzet, M. Maffia and D. Vergara, *Biochim. Biophys. Acta, Mol. Cell Biol. Lipids*, 2019, **1864**, 344–357.
45 O. Piwocka, K. Sterzyńska, A. Malińska, W. M. Suchorska and K. Kulcenty, *Sci. Rep.*, 2025, **15**, 27449.
46 A. K. Mapanao, M. Santi and V. Voliani, *J. Colloid Interface Sci.*, 2021, **582**, 1003–1011.
47 J. Liu, P. Leng and Y. Liu, *Fundam. Clin. Pharmacol.*, 2021, **35**, 86–96.
48 N. Roohani, R. Hurrell, R. Kelishadi and R. Schulin, *J. Res. Med. Sci.*, 2013, **18**, 144–157.
49 N. Abbaspour, R. Hurrell and R. Kelishadi, *J. Res. Med. Sci.*, 2014, **19**, 164–174.
50 J. R. Hunt, C. A. Zito and L. K. Johnson, *Am. J. Clin. Nutr.*, 2009, **89**, 1792–1798.
51 D. G. Barceloux, *J. Toxicol., Clin. Toxicol.*, 1999, **37**, 279–292.
52 H. Schoofs, J. Schmit and L. Rink, *Molecules*, 2024, **29**, 3130.
53 F. Mazuel, A. Espinosa, N. Luciani, M. Reffay, R. Le Borgne, L. Motte, K. Desboeufs, A. Michel, T. Pellegrino, Y. Lalatonne and C. Wilhelm, *ACS Nano*, 2016, **10**, 7627–7638.
54 J. Kolosnjaj-Tabi, Y. Javed, L. Lartigue, J. Volatron, D. Elgrabli, I. Marangon, G. Pugliese, B. Caron, A. Figuerola, N. Luciani, T. Pellegrino, D. Alloyeau and F. Gazeau, *ACS Nano*, 2015, **9**, 7925–7939.
55 A. Quarta, A. Curcio, H. Kakwere and T. Pellegrino, *Nanoscale*, 2012, **4**, 3319–3334.
56 E. Cook, G. Labiento and B. P. S. Chauhan, *Molecules*, 2021, **26**, 6170.
57 B. Issa, I. M. Obaidat, B. A. Albiss and Y. Haik, *Int. J. Mol. Sci.*, 2013, **14**, 21266–21305.
58 S. Bagheri and N. M. Julkapli, *J. Magn. Magn. Mater.*, 2016, **416**, 117–133.
59 H. P. Erickson, *Biol. Proced. Online*, 2009, **11**, 32–51.
60 M. P. Monopoli, C. Åberg, A. Salvati and K. A. Dawson, *Nat. Nanotechnol.*, 2012, **7**, 779–786.
61 A. Lesniak, F. Fenaroli, M. P. Monopoli, C. Åberg, K. A. Dawson and A. Salvati, *ACS Nano*, 2012, **6**, 5845–5857.
62 S. Tenzer, D. Docter, J. Kuharev, A. Musyanovych, V. Fetz, R. Hecht, F. Schlenk, D. Fischer, K. Kiouptsi, C. Reinhardt, K. Landfester, H. Schild, M. Maskos, S. K. Knauer and R. H. Stauber, *Nat. Nanotechnol.*, 2013, **8**, 772–781.
63 C. Bárcena, A. K. Sra, G. S. Chaubey, C. Khemtong, J. P. Liu and J. Gao, *Chem. Commun.*, 2008, 2224–2226, DOI: 10.1039/B801041B.
64 Y. Portilla, Y. Fernández-Afonso, S. Pérez-Yagüe, V. Mulens-Arias, M. P. Morales, L. Gutiérrez and D. F. Barber, *J. Nanobiotechnol.*, 2022, **20**, 543.
65 A. Curcio, G. Curé, A. Espinosa, N. Menguy, I. Galarreta-Rodriguez, A. Abou-Hassan, B. Piquet, L. Motte, Y. Lalatonne, C. Wilhelm and A. Van de Walle, *Small*, 2024, **20**, 2407034.
66 K. Sharma, S. Dey, R. Karmakar and A. K. Rengan, *Cancer Innovation*, 2024, **3**, e102.
67 A. G. Monteduro, S. Rizzato, G. Caragnano, A. Trapani, G. Giannelli and G. Maruccio, *Biosens. Bioelectron.*, 2023, **231**, 115271.
68 Y. Zheng, S. Luo, M. Xu, Q. He, J. Xie, J. Wu and Y. Huang, *Acta Pharm. Sin. B*, 2024, **14**, 3876–3900.
69 M. J. Mitchell, M. M. Billingsley, R. M. Haley, M. E. Wechsler, N. A. Peppas and R. Langer, *Nat. Rev. Drug Discovery*, 2021, **20**, 101–124.
70 S. A. Ejazi, R. Louisthelmy and K. Maisel, *ACS Nano*, 2023, **17**, 13044–13061.
71 I. Hubatsch, E. G. E. Ragnarsson and P. Artursson, *Nat. Protoc.*, 2007, **2**, 2111–2119.